Chemical Science

Cite this: *Chem. Sci.*, 2012, **3**, 1262

www.rsc.org/chemicalscience

EDGE ARTICLE

Fabrication and enhanced photocatalytic activity of inorganic core–shell nanofibers produced by coaxial electrospinning†

Xiaohui Peng,[a] Alexander C. Santulli,[a] Eli Sutter[b] and Stanislaus S. Wong*[ac]

Received 7th July 2011, Accepted 16th January 2012
DOI: 10.1039/c2sc00436d

Despite the interesting properties and potentially exciting applications of multifunctional one-dimensional nanoscale heterostructures that will likely impact areas such as optoelectronics, the fabrication of high-quality one-dimensional coaxial nanostructures in a simple, cost-effective, and scalable manner still remains challenging. Herein, we demonstrate that highly uniform SnO_2/TiO_2 coaxial nanoscale fibers with a tunable internal morphology can be prepared in one step by means of coaxial electrospinning. Specifically, by varying the concentration of the tin precursor solution, the interior of these fibers can be tuned in terms of morphologies, ranging from filled solid to peapod-like, and even to hollow tubes. The diameters of the fiber core and the overall dimensions of the fibers were noted to be in the range of 30–160 and 200–300 nm, respectively, depending upon precursor concentration and electrospinning conditions. In particular, the photocatalytic activity of tubular SnO_2/TiO_2 coaxial nanofibers was found to be higher than that of commercial TiO_2 photocatalysts, an observation which could be attributed to the formation of a seamless heterojunction between SnO_2 and TiO_2 as well as the inherent advantages of a one-dimensional tubular structure. Overall results suggest that coaxial electrospinning can be employed as a novel, facile route for the large-scale synthesis of one-dimensional inorganic coaxial nanoscale heterostructures used for a broad range of applications.

1. Introduction

One-dimensional nanoscale heterostructures have been of particular interest due to their intriguing properties that often go beyond a simple linear sum of their multiple constituent functionalities. Moreover, from both a synthetic and intellectual point of view, the formation of heteroscale junctions is not only incredibly challenging but also simultaneously satisfying. In fact, the most interesting science often occurs at interfaces, especially rationally designed ones which can potentially pit and weave together unusual but often complementary materials into a discrete and chemically distinctive structure. Indeed, the unique properties of these materials, which cannot necessarily be realized in single-component structures, render them attractive in a wide range of applications. These include their incorporation as building blocks in nanoscale electronics as well as in photonics devices,[1] catalysts,[2,3] sensors,[4] as well as solar cells.[5,6]

Not surprisingly, considerable research efforts have been expended towards the synthesis and manufacturing of one-dimensional heterostructures possessing various chemical compositions, including components consisting of metals[2,3] and semiconductors.[7–15] In general, a core–shell heterostructure can be generated by two-step synthetic protocols, wherein the initial one-dimensional core template is pre-synthesized prior to the subsequent shell coating.[9,12,14] However, such approaches based upon solution-phase manipulations often require either (a) tedious purification steps in order to obtain pure core materials and/or (b) a very careful experimental design in order to efficaciously apply a secondary homogeneous, contiguous coating of shell materials. Alternatively, epitaxial growth based upon a two-step deposition process, employing either chemical vapor deposition,[1,7,16] pulsed laser deposition,[8,11] or atomic layer deposition[5] techniques can provide the heterostructure with a well-defined and clean interface. However, these gas-phase processes usually require highly specialized equipment in order to achieve the high temperatures and/or low vacuum environments that are needed; such an approach therefore can be potentially be energy-intensive and expensive. By contrast, simpler template-assisted methods usually are low-throughput in nature and can also be costly and time-consuming in terms of mass generation of product. Furthermore, judicious exploitation of known chemical conversion processes (*e.g.* sulfidation[17] and the Kirkendall effect[18]) has been successfully used for the preparation of

[a]*Department of Chemistry, State University of New York at Stony Brook, Stony Brook, NY, 11794-3400, USA. E-mail: sswong@notes.cc.sunysb.edu; sswong@bnl.gov; Fax: +631-344-3178; Tel: +631-032-1703*
[b]*Center for Functional Nanomaterials, Brookhaven National Laboratory, Building 735, Upton, NY, 11973, USA*
[c]*Condensed Matter Physics and Materials Sciences Department, Brookhaven National Laboratory, Building 480, Upton, NY, 11973, USA*
† Electronic supplementary information (ESI) available. See DOI: 10.1039/c2sc00436d

core–shell heterostructures. However, such strategies are highly limited in scope as they depend upon the precise nature of the materials synthesized. Moreover, the viability of additional two-step synthetic protocols, based upon a combination of the methods discussed above, is usually hampered by inherent limitations associated with individual techniques.[19,20] As such, developing generalizable and facile practical protocols that will allow for the fabrication of one-dimensional well-defined core–shell nanostructures consisting of two materials of often very distinctive chemical compositions using simple and scalable methods, still poses a significant synthetic challenge.

Electrospinning has been of interest as it is a relatively simple, environmentally friendly, reasonably energy efficient, and versatile technique for generating highly uniform one-dimensional nanofibers composed of a variety of materials including polymer and inorganic composites.[21–23] Its attractive advantages include not only its high throughput in a continuous process under mild conditions but also its inherent flexibility in terms of controlling the fiber diameter from the micron to nanometre scales. Electrospun inorganic nanofibers including TiO_2, ZnO, V_2O_5, and Fe_3O_4 not only possess the unique properties of the individual materials themselves but also incorporate outstanding attributes associated with the one-dimensional morphology.[24,25] Moreover, in recent years, the state-of-the-art configuration of the nozzle has advanced in a way such that the structure and morphology (and hence, overall functionality) of the resulting nanofibers can be precisely altered. For example, the coaxial nozzle has been developed, allowing for the simultaneous coaxial electrospinning of two distinctive components.[26] This technique stands out from other methods, owing to its ability to very easily prepare one-dimensional core–shell nanoscale heterostructures on a large scale in a one-step synthetic process. To date, electrospun polymer nanofibers with either core–shell or tubular structures have been fabricated[27] for a wide variety of applications including drug delivery devices[28,29] and electrodes.[30] However, to the best of our knowledge, a one-step fabrication of inorganic nanofibers with both a well-defined core–shell structure and a tunable internal morphology (*e.g.* from hollow cavities to filled channels) using coaxial electrospinning has not as yet been reported.

TiO_2, as a well-known photocatalyst, has been widely used for the treatment of organic pollutants in water and air.[31] However, the drawback of TiO_2 photocatalysts is that the rate of electron transfer from TiO_2 to either oxygen or the electron acceptor on the surface of TiO_2 is much slower than that of the recombination of the electron–hole pair, a fact which impairs the photocatalytic activity of TiO_2.[31] To address this problem, coupling TiO_2 with another component, either a semiconductor or a metal, has been proposed as a means of preventing charge carriers from fast recombination by achieving efficient charge separation between TiO_2 and the other material. Among coupled semiconductor photocatalysts, the TiO_2/SnO_2 system in particular has been extensively studied, as it has demonstrated high photocatalytic activity due to fast electron transfer from TiO_2 to SnO_2.[32–35] SnO_2 is a common semiconductor used as a component of transparent conductors, electrodes, and sensors, due to its excellent conductivity.[36,37] The band-gap energies of TiO_2 and SnO_2 are 3.2 and 3.8 eV, respectively. Hence, the energy offset between TiO_2 and SnO_2 allows photogenerated electrons to accumulate onto SnO_2 whereas holes will accrue onto TiO_2 upon formation of a heterojunction at the TiO_2/SnO_2 interface (Scheme 1).

Various TiO_2/SnO_2 binary oxide nanostructures have been prepared including films,[35,38] nanoparticles,[39–41] nanotubes,[32] and nanowires.[8] However, one-dimensional nanostructures in particular have attracted a significant amount of interest, because of their higher aspect ratios, large surface area-to-volume ratios, and potentially high conductivity. Studies have shown that well-ordered nanoparticles encapsulated within one-dimensional nanofibers can facilitate interparticle charge transfer along the nanofiber framework as compared with randomly packed nanoparticles.[21,24] Moreover, apart from the necessity for reasonable interfacial contact between TiO_2 and SnO_2 for efficient charge separation, it is believed that full exposure of both components to the reaction medium would allow for both photogenerated holes and electrons to take part in the photocatalytic reactions, thereby enhancing the observed photocatalytic efficiency. In order to achieve this requirement, a bi-component nanowire structure of TiO_2 and SnO_2 has been realized by electrospinning with a side-by-side dual spinneret.[33] However, the fragile nature of this side-by-side design may result in poor catalyst durability, an essential property for catalysts. In order to mitigate this potentially damaging flaw, a core–shell architecture is more preferable, owing to its greater stability and larger interfacial contact.

In this work, we have demonstrated that core–shell SnO_2/TiO_2 nanofibers can be successfully fabricated in one simple step by means of coaxial electrospinning, thereby eliminating the need for any secondary deposition step. This simple, straightforward method yields highly uniform coaxial nanoscale heterostructures with well-defined interfaces between components. By rationally and precisely controlling materials synthesis parameters and electrospinning conditions, the resulting morphology of coaxial SnO_2/TiO_2 nanofibers can be altered as either tubular coaxial, peapod-like, or solid coaxial architectures. Furthermore, due to the interesting electronic properties of SnO_2 and TiO_2 discussed above, the resulting core–shell nanofibers, incorporating both

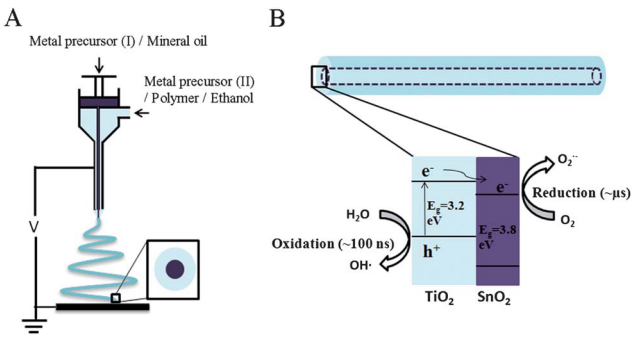

Scheme 1 (A) A simple schematic illustration of the experimental set-up associated with co-axial electrospinning. The core solution is fed into the inner spinneret while the shell solution is transported into the outer one. Coaxial fibers are collected on the metal substrate under high voltage conditions. (B) The cartoon represents a typical configuration of the tubular SnO_2/TiO_2 coaxial electrospun fibers. The corresponding energy band diagram of SnO_2 and TiO_2 illustrates the principle of charge separation at the interface of SnO_2/TiO_2 as well as the subsequent photocatalytic reaction.

materials, can potentially be used as promising materials for photon energy conversion applications, including as solar devices and photocatalysts.

In particular, we have tested the photocatalytic activity of our novel tubular SnO_2/TiO_2 coaxial heterostructure fibers generated in this study. The enhanced photocatalytic activity of our tubular SnO_2/TiO_2 systems as compared with commercial TiO_2 photocatalysts can be attributed to a number of factors: (i) the dual layer structure ensures a well-defined heterojunction between TiO_2 and SnO_2, which allows for an increase in charge-separation efficiency; (ii) one-dimensional nanofibers facilitate efficient interparticle charge transfer along the nanoscale fiber framework; and (iii) the hollow structure allows for full exposure of both the TiO_2 outer-layer and SnO_2 inner-layer to the reaction medium, thereby allowing for both photogenerated electrons and holes to participate in the photocatalysis reaction. Hence, due to the versatility in our choice of materials as well as the flexibility of morphology control, our work has demonstrated that coaxial electrospinning can be considered to be an excellent and facile alternative route towards the fabrication of one-dimensional coaxial heterostructures with different compositions and configurations, thereby providing the opportunity for the development of unique nanoscale devices. In particular, tubular coaxial structures prepared by coaxial electrospinning, which cannot be easily obtained by conventional synthetic routes, would be significantly beneficial for a broad range of applications, where it is desirable to have access to both materials, while maintaining a large and stable interface.

2. Experimental section

2.1. Materials

Titanium isopropoxide (98+%), poly(vinyl pyrrolidone), and mineral oil (Lot A0251014) were purchased from Acros Organic. Tin ethylhexanoate (96%) was obtained from Alfa Aesar.

2.2. Preparation of TiO_2 and SnO_2 precursor solutions

The TiO_2 electrospinning solution was prepared by first dissolving 0.175 g of poly(vinyl pyrrolidone) (PVP) (M_w = 1 300 000) in 2 mL of ethanol with stirring, followed by the addition of 0.5 mL of acetic acid. Once the PVP was completely dissolved and the solution became transparent, 0.25 mL of titanium isopropoxide, $Ti(OiPr)_4$, was added and kept stirring in solution in order to obtain a homogeneous solution with a final concentration of Ti at 3×10^{-4} mol mL^{-1}. Subsequently, the precursor solution was loaded into a 3 mL plastic syringe. SnO_2 precursor solutions with varying concentrations were prepared by adding selective aliquots of tin ethylhexanoate to light mineral oil (LMO), followed by stirring in order to create a homogeneous solution. The precursor solution was also loaded into a separate 3 mL plastic syringe.

2.3. Electrospinning

In order to fabricate co-axial fibers, a home-made dual spinneret with coaxial geometry was used, as shown in Scheme 1A. In a typical experiment, the TiO_2 precursor solution was fed into the outer 16 G spinneret with a feeding rate of 1.0 mL h^{-1}. At the same time, the SnO_2 precursor solution was run into the inner 23 G spinneret with a feeding rate of 0.1 mL h^{-1}. A high voltage was applied between the tip of the spinneret and the aluminum foil collector with a voltage/distance profile in the range of 5 kV/3 inch. As-spun nanofibers were left to 'air dry' for one day in order to allow for the hydrolysis of $Ti(OiPr)_4$ to proceed to completion, followed by calcination in air at 500 °C for 2 h. All as-generated nanofibers were prepared under identical electrospinning conditions, unless otherwise noted.

2.4. Characterization

Crystallographic and purity information on the prepared nanofibers were obtained using a Scintag diffractometer, operating in the Bragg configuration using Cu-Kα radiation (λ = 1.54 Å). Scanning electron microscopy (SEM) images were processed with a field emission (FE) SEM instrument (Leo 5050), operating at an accelerating voltage of 20 kV and equipped with energy dispersive X-ray spectroscopy (EDS) capabilities. High-resolution TEM (HRTEM) images and selected area electron diffraction (SAED) patterns were gathered using a JEOL 2010F instrument, equipped with a Gatan high-angle annular dark field detector (HAADF) for performing either incoherent HAADF or Z-contrast imaging in scanning TEM mode at accelerating voltages of 200 kV. Specimens for cross-sectional TEM experiments were prepared by embedding samples in Epon resin, which was then cut by a Reichert-Jung UltracutE ultramicrotome and placed onto Formvar-coated copper grids. N_2 absorption–desorption profiles were measured with a NOVA 2200e Surface Area & Pore Size Analyzer in order to determine the surface area of the electrospun fibers. Pore sizes for each sample were calculated, according to Barrett–Joyner–Halenda (BJH) theory.

2.5. Photocatalytic degradation activity

In typical experiments, 4 mg of either tubular SnO_2/TiO_2 nanofibers, peapod-like SnO_2/TiO_2 nanofibers, solid SnO_2/TiO_2 nanofibers, TiO_2 nanofibers, or commercial TiO_2 nanoparticles (Degussa P25) were dispersed, by sonication for 5 min, in separate aqueous solutions of 5 mg L^{-1} Rhodamine B (RhB). The solutions were magnetically stirred in the dark for 30 min so as to establish an adsorption–desorption equilibrium of reactants with the photocatalysts. We note that during the entire duration of each photocatalytic measurement, the as-prepared organic dye solution containing the appropriate photocatalyst was homogeneously stirred in order to prevent these photocatalyst samples from undergoing unwanted sedimentation. Upon exposure to UV light ($\sim$3 mW cm^{-2}) at 366 nm, the UV-visible absorption spectra of RhB were monitored at different time intervals. At each time point, 1 mL of solution was withdrawn and centrifuged in the dark to quell further reactivity. Aliquots of the clear dye supernatant were then carefully withdrawn and subsequently placed into a quartz cuvette for UV-visible measurements. Specifically, the photocatalytic performance of each type of photocatalyst was evaluated by measuring the change in the intensity of the optical absorbance peak at 555 nm. In terms of a control experiment, an RhB solution was treated under identical conditions without the addition of any photocatalysts.

3. Results and discussion

3.1. Crystal structure of SnO_2/TiO_2 nanofibers

The crystallographic information associated with SnO_2/TiO_2 nanofibers has been investigated by XRD. As illustrated in Fig. 1a, the pure TiO_2 nanofibers, calcined at 500 °C, exhibited a pure anatase phase (JCPDS No. 21-1272), whereas the pure rutile phase of TiO_2 nanofibers could be obtained upon calcination at 800 °C (Fig. 1b). Surprisingly, the calcined SnO_2/TiO_2 nanofibers possessed a pure rutile phase for both SnO_2 and TiO_2 components, even at a relatively low calcination temperature of 500 °C. All peaks in fact could be indexed to the tetragonal rutile phase of TiO_2 (JCPDS No. 21-1276) and SnO_2 (JCPDS No. 72-1147), as shown in Fig. 1c. As the peaks corresponding to rutile TiO_2 lie very close to those of rutile SnO_2, the observed peak pattern of SnO_2/TiO_2 was broader than that associated with their individual constituent components. A phase transition of TiO_2 from the anatase phase to the rutile phase, which can plausibly be ascribed to the doping of Sn^{4+} ions, has been previously reported.[39,42] In our case, we speculate that some Sn^{4+} ions might have migrated into the Ti–O–Ti network during the electrospinning and subsequent calcination processes. This latter step could then have enabled and facilitated further diffusion of tin ions at the interface and inside the Ti–O–Ti network, thereby inducing the phase transition of TiO_2 at the relatively low temperature we observed.[42] It also has been found that rutile SnO_2 can promote the preferential growth of rutile TiO_2, owing to the fact that the lattice difference between rutile SnO_2 and TiO_2 is only about 2%.[43] Hence, the influence of the SnO_2 lattice could likely be another important factor in promoting the observed phase transition of TiO_2.

3.2. Effect of concentration of tin precursor solution upon the internal morphology of electrospun SnO_2/TiO_2 nanofibers

In order to create a distinctive boundary between the core and shell materials, it has been previously suggested that physical mixing between two solutions during the electrospinning process should be eliminated by using two immiscible solvents for the core solution and the shell solution, respectively.[44] Hence, in our study, ethanol was chosen as the solvent for the shell precursor solution whereas LMO, which is not miscible with ethanol, was used for the core precursor solution. The morphologies of the resulting SnO_2/TiO_2 nanofibers have been evaluated by SEM with a backscattering detector, whereas titanium and tin elements could be distinguished by the differential contrast in these images owing to their substantial difference in atomic number.

We have noted that the concentration of tin precursor solution maintains a significant influence upon the internal morphology of the resulting SnO_2/TiO_2 coaxial fibers, as summarized in Scheme 2. Specifically, highly uniform SnO_2/TiO_2 nanofibers with unique tubular coaxial structures can be formed when the concentration of tin(II) precursor solution is 1.6 mmol mL^{-1}. As shown in Fig. 2A and B, a smooth thin layer was found to coat the interior wall of the tubular nanofibers possessing an overall outer diameter of 285 ± 45 nm and an inner diameter of 122 ± 36 nm; this thin layer was continuous along the entire inner surface of fibers. A cross-sectional SEM image (inset) of fractured nanofibers unambiguously shows an integral bright ring, concentric with the hollow outer fiber.

In addition, the cross-sectional TEM image along with the corresponding EDS line scan across the structure confirmed the overall elemental distribution in our typical samples. Specifically, Fig. 2C highlights a representative cross-sectional TEM view of a single discrete nanofiber, wherein an inner concentric SnO_2 layer, consisting of densely packed nanoparticles, with a diameter of 20 ± 5 nm, was observed within the elementally less-dense but thicker circular TiO_2 shell. Particle-like aggregates in the hollow central core region most likely corresponded to the

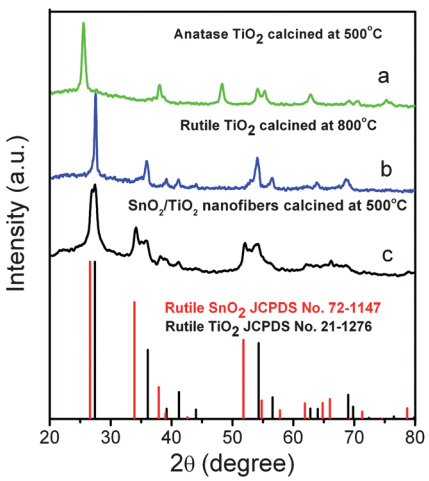

Fig. 1 XRD patterns of TiO_2 fibers sintered at 500 °C (a) and 800 °C (b), as well as of hollow SnO_2/TiO_2 coaxial nanofibers (c).

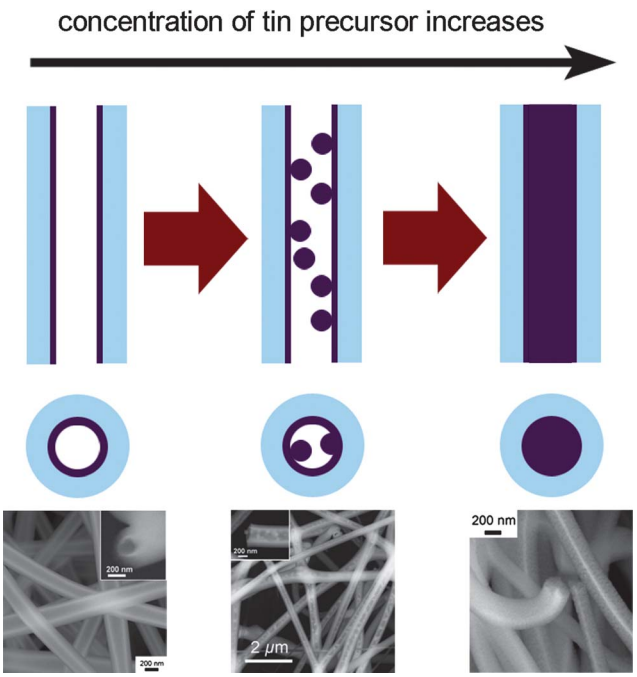

Scheme 2 Effect of the concentration of tin precursor upon the morphology of the SnO_2/TiO_2 electrospun fibers. By increasing the concentration of tin precursor, the morphology of electrospun fibers evolves from a tubular coaxial structure to a peapod-like structure, and finally, onwards to a solid, filled core–shell structure.

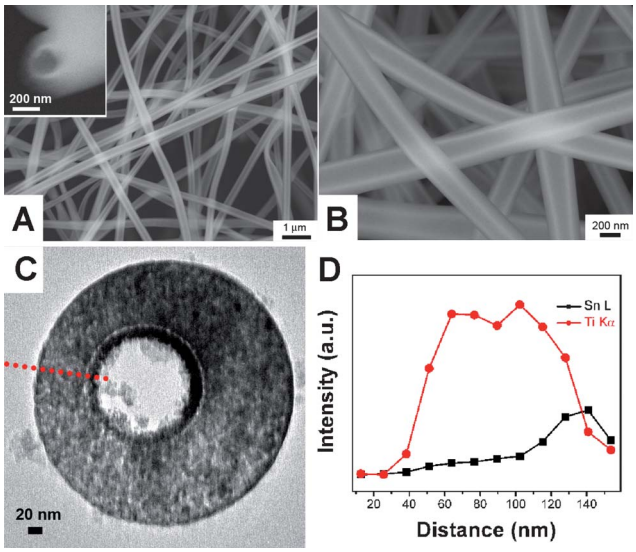

Fig. 2 (A, B) SEM images of hollow SnO_2/TiO_2 coaxial nanofibers obtained when the concentration of tin(II) precursor is 1.6 mmol mL^{-1}. Inset is an SEM image of a typical cross-sectional view of hollow SnO_2/TiO_2 coaxial nanofibers. (C) Cross-sectional TEM image of coaxial SnO_2/TiO_2 core–shell nanofibers. (D) The signal intensity profile of Sn L and Ti Kα derived from EDS line scanning profiles collected along the red dotted line in (C). Each data point corresponds to the red dot along the line drawn from left to right across the image.

fragments of fibers generated during the sample preparation. The size of the inner hollow region is 141 nm, consistent with the results obtained from the SEM images. In addition, the outer TiO_2 shell consists of loosely packed small nanoparticles with diameters of about 15 nm, indicative of the polycrystallinity of the nanofibers. The EDS line scan results (Fig. 2D), collected from the area indicated by the red dotted line in Fig. 2C, showed that the intensity of the Sn L signal reached a maximum in the inner layer region whereas the Ti Kα signal profile dramatically increased at the location of the outer shell, in excellent agreement with SEM observations. All of these observations are consistent with the formation of tubular TiO_2 nanofibers consisting of a thin inner layer of SnO_2.

Such a structure has potential, attractive advantages in terms of applications associated with sensing, catalysis and energy conversion, because it possesses not only a well-defined heterojunction comprised of two distinctive, tunable, components but also an open inner channel which provides for high surface area and also direct access to the interior material. Not surprisingly, this unusual architecture gave rise to superior photocatalytic activity, as compared with the application of either the individual single-component analogues or its solid wirelike-structure counterparts, as will be further elaborated upon in a later section. Importantly, to the best of our knowledge, such tubular coaxial nanofiber structures consisting of two distinctive metal oxides fabricated by coaxial electrospinning have not been previously reported.

When the concentration of the tin(II) precursor solution was increased to 2.2 mmol mL^{-1}, we begin to see the formation of SnO_2 nanoparticles within the inner cavity of the nanowires. Representative SEM images, namely Fig. 3A and B, highlight the presence of these nanoparticles, and reveal their sizes to be 58 ± 13 nm. These peapod-like structures maintain overall widths of 284 ± 36 nm, similar to those of the hollow nanotubes. However, they possess a slightly decreased inner cavity, measuring only 99 ± 16 nm. We attribute this reduction of the inner cavity size to the proportionally lower LMO content in the tin precursor solution. In order to verify that the observed SnO_2 nanoparticles were in fact inside the tubular fibers, as opposed to on the external surface of TiO_2 nanofibers, SEM images of the same sample area were taken under different accelerating electron voltages. In principle, an increase in accelerating electron voltage allows us to visualize regions within the fiber interior.

As illustrated in Fig. 3C, nanofibers with a smooth exterior were observed at an accelerating voltage of 10 kV, whereas the hollow features as well as nanoparticles themselves became more readily apparent upon increasing the accelerating voltage to 20 kV (Fig. 3D). These results confirmed that SnO_2 nanoparticles were likely encapsulated within the tubular fibers themselves, and not simply physically affixed onto the exterior surface of the fibers. Additional proof was provided using cross-sectional HRTEM. A representative image (Fig. 3E) shows a typical structure of peapod-like SnO_2/TiO_2 nanofibers. Specifically, the size of the particle aggregate attached to the interior wall of fibers was about 70 nm, consistent with findings from SEM. Aggregates were composed of smaller nanoparticles, measuring ~12 nm. In addition to these nanoparticles, the thin inner SnO_2 coating, present within the hollow nanotubes, is maintained within these peapod-like nanostructures. This is indicative that

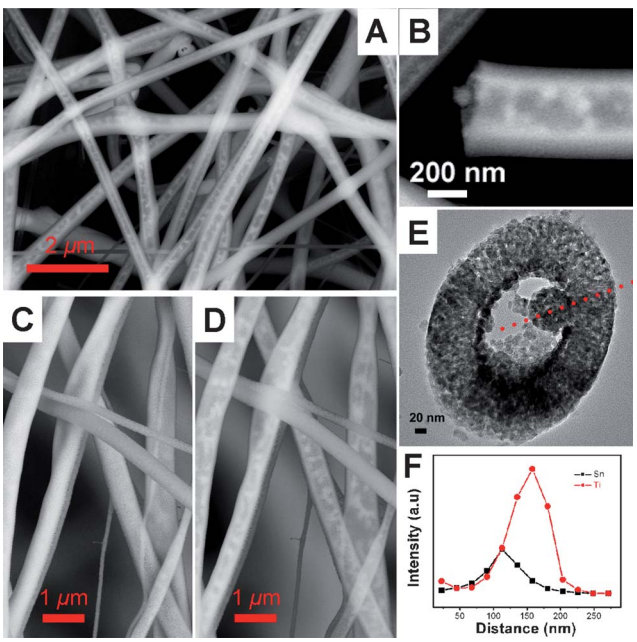

Fig. 3 (A and B) SEM images of peapod-like SnO_2/TiO_2 nanofibers created when the concentration of tin(II) precursor is 2.2 mmol mL^{-1}. SEM images of the same sample area were taken at accelerating electron voltages of 10 kV (C) and 20 kV (D), respectively. (E) Cross-sectional TEM image of peapod-like SnO_2/TiO_2 nanofibers, illustrating particle-like features attached to the inner hollow wall of the fibers. (F) The signal intensity profile of Sn L and Ti Kα derived from EDS line scanning profiles collected along the red dotted line in (E). Each data point corresponds to the red dot along the line drawn from left to right.

upon the formation of a contiguous inner coating of SnO_2 within the nanostructures, any excess tin precursors were noted to begin to fill in the actual inner pore structure. An EDS line scan result (Fig. 3F) again demonstrated that Sn was localized in the region of the inner particle, whereas the Ti signal was far more dominant in the outer shell area, in spite of the sample drifting caused by charging, as well as the interference associated with the fragments of fibers generated during the sample preparation.

We analyzed another characteristic peapod-like SnO_2/TiO_2 nanofiber sample, as shown in Fig. 4A. A highly magnified HRTEM image of a representative interface (Fig. 4B) between the TiO_2 and SnO_2 regions in a selected segment of these peapod-like architectures is shown in Fig. 4E. Both oxides as well as the interface between them exhibit a polycrystalline structure, as further confirmed by the corresponding diffraction patterns (Fig. 4C and D). The images spanning that interface clearly indicate that this typical boundary between the two oxide structures is composed of constituent particle grains measuring 10–20 nm in size. The boundary between the two oxides, as highlighted by the clear spatial differentiation between Sn and Ti signals shown in the EDS map in Fig. 4F, is very sharp and well defined and moreover, appears to be less dense than the surrounding phases. The SnO_2 region can be clearly distinguished, as it shows somewhat darker contrast in the TEM images, which can be correlated with an area with higher Sn content in the corresponding EDS map (Fig. 4F). The diffraction patterns of TiO_2 (Fig. 4C) and SnO_2 (Fig. 4D) are essentially identical, which suggests that there might be an easy epitaxy (not involving strain) between them and, indeed, in the HRTEM image, some lattice planes are seen to continue across and traverse the boundary between the two oxide grains at the interface. This observation indicates a relationship between the grains at the interface even though one cannot exactly establish the presence of an epitaxial growth upon heating, which normally would have involved the formation of two monocrystalline phases between the two "polycrystalline" materials. Nonetheless, our results are undoubtedly consistent with the formation of a number of naturally existing grain boundaries between the two oxides which are well separated compositionally.

Upon application of the tin precursor without the addition of mineral oil, we were able to form solid, filled nanostructures of SnO_2/TiO_2 coaxial nanofibers. Typical SEM images of as-prepared SnO_2/TiO_2 core–shell nanofibers are shown in Fig. 5A and B. Nanofibers, possessing a diameter of 275 ± 30 nm, maintained a highly uniform one-dimensional nature with a discernible core–shell structure, with an average core size of 53 ± 13 nm. The contrast noted in the SEM images arising from the difference in the atomic number between Sn and Ti highlights a clearly distinctive boundary between the shell and the core, which is continuous along the entire length of fibers. Particularly,

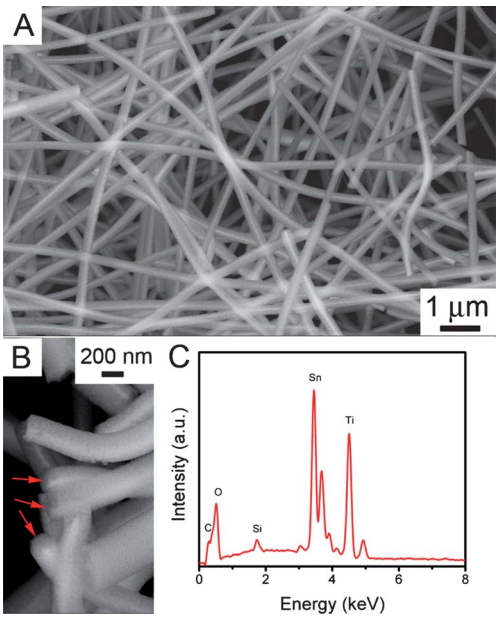

Fig. 5 (A) Low-magnification SEM image of highly uniform SnO_2/TiO_2 core–shell nanofibers generated when the concentration of tin(II) precursor is 3.0 mmol mL^{-1}. (B) High-magnification SEM image of SnO_2/TiO_2 core–shell nanofibers. Red arrows indicate the presence of fractured fibers, wherein the core shell structure can be clearly observed. (C) EDS profile collected from the SnO_2/TiO_2 core–shell nanofibers.

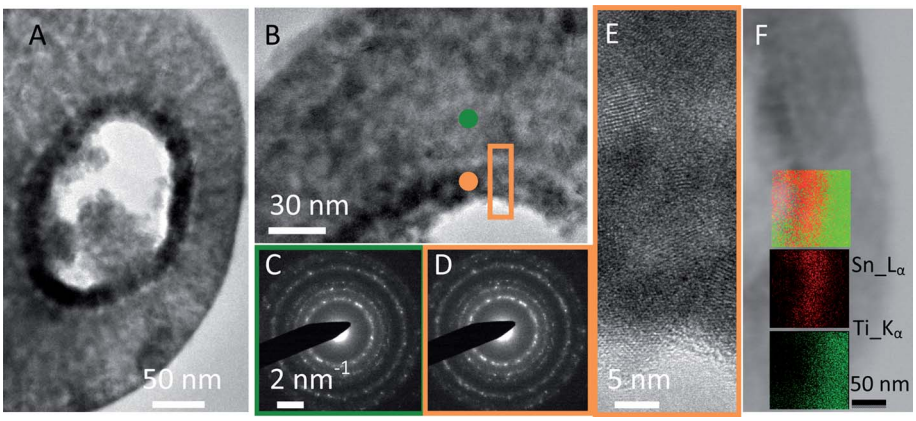

Fig. 4 (A-B) HRTEM image illustrates a typical interface between the TiO_2 and SnO_2 regions in a selected segment of a representative peapod-like SnO_2/TiO_2 core shell nanofiber. (E) A highly magnified HRTEM image of the interface corresponding to the orange rectangle in (B). SAED data taken from the regions designated by the green (C) and orange (D) areas, respectively. Accompanying EDS map (F) superimposed upon the actual area of the sample where it was acquired. Beneath the composite EDS map, the individual Sn and Ti maps are shown.

in the image (Fig. 5B) where the fibers were fractured and the cross sections of the fibers themselves can be visualized, it is evident that the bright central core is entirely and concentrically wrapped by the shell materials. Elemental analysis using the EDS spectrum associated with SEM images is shown in Fig. 5C, indicating that the fibers contain both Ti and Sn without the presence of any distinguishable impurities.

Fig. 6A shows a typical cross-sectional TEM view of these particular SnO_2/TiO_2 nanofibers, suggesting that the fibers were composed of a thick shell, consisting of essentially loosely packed nanoparticles with an average diameter of about 20 nm and a denser circular central core with a size of about 50 nm, in good agreement with the SEM image data. The loosely packed particles in the shell likely gave rise to the overall porosity of these SnO_2/TiO_2 nanofibers, an observation which is potentially beneficial for their applicability in photocatalysts and in solar cells. EDS spectra (Fig. 6B) were taken at selected areas of the shell and core, respectively. As expected, the strong Sn signal collected from the center area confirmed that the core of nanofibers was primarily comprised of SnO_2, whereas the shell was dominated by the presence of Ti, indicative of the TiO_2 shell. Interestingly, we also noted that a Sn signal, albeit significantly weaker, in the shell region, consistent with the idea that Sn is doping TiO_2.

The electron diffraction patterns of the selected sections of the core and shell regions (*i.e.* Fig. 6C and D), respectively, indicate that both the core and shell of SnO_2/TiO_2 nanofibers are polycrystalline, consistent with the presence of grain boundaries, and that the five most distinctive diffraction rings of the core (or shell) can be assigned, moving concentrically and sequentially from the center outwards, to the (110), (101), (200) (or (111)), (211), and (301) planes of rutile phase SnO_2 (or TiO_2). In addition, the discernible lattice fringes of nanoparticles observed in both the shell and core areas were indicative of their high crystallinity (Fig. 6C and D) though there was no conclusive evidence of either any preferred lattice orientation or any epitaxial growth associated with the different crystallites. The fringe spacing has been determined to be 3.30 Å for the shell materials, a value which is only slightly larger than the expected $d_{110} = 3.25$ Å associated with phase-pure rutile TiO_2.[39] This slight lattice expansion may be partially attributed to Sn doping of TiO_2, whose likelihood had already been implied by the aforementioned XRD and EDS results.

3.3. Effect of electrospinning conditions upon the morphology of SnO_2/TiO_2 electrospun nanofibers

The subtle influence of other factors such as feeding rate and the applied voltage upon the morphologies of SnO_2/TiO_2 nanofibers was also investigated. By contrast with the importance of the concentration of the tin(II) precursor solution upon structure, changing either the feeding rate or applied voltage does not appear to essentially impact upon the inherent morphologies of SnO_2/TiO_2 nanofibers. Nonetheless, as the feeding rate necessarily affects the precursor supply during the electrospinning process, that factor can play an important role in determining the resulting dimensions of the fibers obtained. Indeed, the size of the inner diameter of nanofibers increases directly as a function of the inner feeding rate, as summarized in Tables 1 and 2. In the case where the concentration of the tin(II) precursor solution was 1.6 mmol mL^{-1} with an inner feeding rate of 0.15 mL h^{-1}, the hollow co-axial structure was retained, whereas the diameter of the inner cavity increased in magnitude by 134% to 164 ± 43 nm as compared with only 122 ± 36 nm when the tin precursor feeding rate used was 0.10 mL h^{-1}. Similarly, when the inner feeding rate was further decreased to ~0.03 mL h^{-1}, the overall

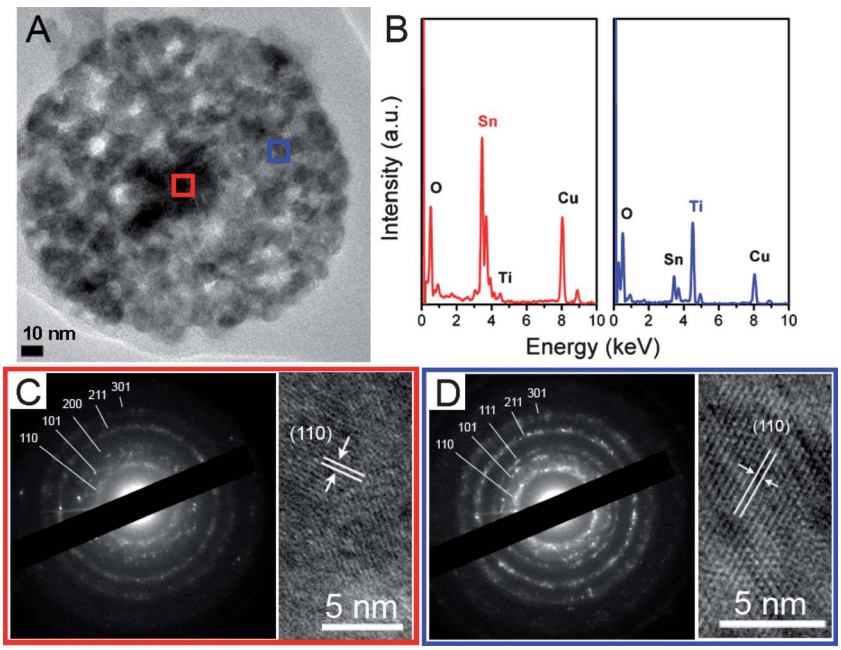

Fig. 6 Cross-sectional TEM image (A) of a representative SnO_2/TiO_2 core shell nanofiber, prepared at a concentration of tin(II) precursor of 3.0 mmol mL^{-1}. (B) EDS profiles collected from the corresponding frames indicated in the TEM image. (C) SAED and HRTEM data obtained from the core component. (D) SAED and HRTEM taken from the shell region.

Table 1 The influence of inner tube feeding rate upon the resulting dimensions of as-prepared tubular TiO_2/SnO_2 nanofibers

Feeding rate/mL h^{-1}		Diameter/nm	
Outer needle	Inner needle	Inner tubes	Fibers
1.0	0.15	164 ± 43	301 ± 50
	0.10	122 ± 36	285 ± 45
	0.03	60 ± 16	236 ± 23

Table 2 The influence of feeding rate upon the resulting dimensions of TiO_2/SnO_2 nanofibers

Feeding rate/mL h^{-1}		Diameter/nm	
Outer needle	Inner needle	Cores	Fibers
2.0	0.20	63 ± 19	345 ± 54
1.0	0.10	53 ± 13	275 ± 30
	0.05	32 ± 5	236 ± 23
0.5	0.05	37 ± 7	194 ± 20

diameter of the fibers as well as their inner cavity diameter diminished to 236 nm and 60 nm, respectively.

It is also worth mentioning that at a constant feeding rate of the shell precursor solution, a minimum feeding rate of the core precursor solution, within a certain range, was required in order to ensure formation of nanoscale fibers with continuous inner features. For example, if the inner shell feeding rate were too low, *i.e.* below 0.03 mL h^{-1}, shorter hollow segments could potentially form inside each of the fibers.[44] On the other hand, if the inner oil-phase solution were injected at a substantially high rate, for example, 0.5 mL h^{-1} in our case, no fibers were collected, as the supply of shell precursor solution would not have been sufficient to completely coat the oil phase with shell material during electrospinning. Similarly, solid SnO_2/TiO_2 nanofibers exhibited the same trend in that a decrease in the inner feeding rate can lead to a corresponding decrease in the diameter of the core and in the overall dimension of the as-produced fibers. The reduction in the dimension of fibers correlated with a decrease in the outer feeding rate as well. Therefore, in this study, we were able to vary the core diameter of solid SnO_2/TiO_2 nanofibers in the range of 30–60 nm by correspondingly altering the inner feeding rate between 0.05–2 mL h^{-1}.

By contrast with the substantial effect of feeding rate upon the resulting fiber diameter, the magnitude of the applied voltage was found to exert little if any influence upon the dimensions of fibers synthesized under our experimental conditions (Table 3). Specifically, at a given feeding rate, the average diameter of fibers varied within a relatively narrow range of 272 to 285 nm, whereas the inner diameter slightly widened from 104 to 122 nm when the applied voltage was reduced from 7 to 5 kV. Previous studies[44] have demonstrated that the enhancement of local electrical field can result in a significant decrease in fiber diameter when fibers with a single composition are fabricated. In our case herein, the magnitude of the electrical field was limited to a relatively narrow range of 5–7 kV in order to achieve the formation of a stable co-axial jet, that would ultimately yield co-axial fibers. We noted that below the minimum voltage of the critical range necessary to form the electrospun fibers, the reagent solutions tended to drip haphazardly from the spinnerets without the formation of a fiber jet. By contrast, the use of voltages above the critical range would cause recession of the Taylor cone, which would therefore inhibit production of a co-axial jet. In fact, we have noted that our considerably limited ability to vary the applied voltage in our case precluded us from deducing a definitive relationship between the magnitude of the electrical field and the resulting fiber dimension.

Table 3 The influence of the voltage profile upon the resulting dimensions of tubular TiO_2/SnO_2 nanofibers

Voltage/kV	Diameter of inner tubes/nm	Overall diameter of fibers/nm
5	122 ± 36	285 ± 45
6	104 ± 23	280 ± 48
7	104 ± 25	272 ± 37

3.4. Plausible mechanism

In a previous study, a structure with SnO_2 nanoparticles encapsulated inside the hollow TiO_2 nanofibers was reported.[45] However, the unique tubular structure with dual co-axial layers formed in our study has not been reported before. We note that tin ethylhexanoate as the tin precursor in our study has an appealing solubility, due to its distinctive structure. It is an amphiphilic molecule consisting of a hydrophobic alkyl chain terminal group as well as a hydrophilic carboxylate terminal group, allowing it to dissolve and/or disperse in both nonpolar and polar solvents. A simple test performed by adding ethanol to a mixture of tin 2-ethylhexanoate and mineral oil showed that the tin precursor dispersed in mineral oil gradually accumulated at the interface between the ethanol layer and mineral oil layer, forming an intermediate layer (Fig. S1, ESI†). As such, it is highly likely that tin ethylhexanoate molecules migrate to the interface between the polar shell solution (ethanol) and the nonpolar core solution (mineral oil) during electrospinning prior to decomposition into SnO_2 under the heating treatment. Moreover, while the as-prepared fibers were air-dried at room temperature, allowing for hydrolysis of the titanium precursor, and subsequently heated at elevated temperature for annealing, small TiO_2 nanocrystals started to grow in the shell. Those TiO_2 nanocrystals could potentially provide active sites for the heterogeneous nucleation of SnO_2 since the carboxylate group of ethylhexanoate molecules in the tin precursor is apt to anchor onto the surface of TiO_2.[46] Upon calcination, the metal precursors would then be converted into robust metal oxide layers, whereas the polymer and mineral oil would be removed. It is highly likely that the growth of metal oxide nanocrystals occurred simultaneously with, if not prior to, the combustion of polymer and mineral oil. Hence, even though the calcination step led to the shrinkage of the overall dimension of fibers, the tubular structure was still retained.

In addition, the proportion of mineral oil within the tin precursor solution plays a key role in forming the tubular co-axial SnO_2/TiO_2 structure. For instance, a decrease in the concentration of tin precursor to 0.8 mmol mL^{-1}, a move which

would necessarily increase the proportion of mineral oil, resulted in the formation of "bead-like" fibers consisting of wider central cavities coated with a discontinuous inner SnO_2 layer (Fig. S2, ESI†). Since mineral oil cannot be readily electrospun, in this case, the shell solution may not effectively confine and contain the core solution within the co-axial cone, due to the fact that an increase in the proportion of mineral oil may reduce the interfacial stress generated between the core solution and shell solution in the co-axial Taylor cone. As a result, the inner jet can then undergo various break-up processes, leading to the formation of hollow bead fragments interconnected by solid fibers.[47] By contrast, an increase of the concentration of tin precursor to 1.6 mmol mL^{-1} provided for sufficient tin precursor materials to coat the inside wall of the tubular TiO_2, thereby resulting in the formation of the tubular co-axial SnO_2/TiO_2 structure we have observed. When the concentration of tin precursor was subsequently increased to 2.2 mmol mL^{-1}, the use of an excess amount of tin precursors led to the formation of SnO_2 nanoparticles in addition to the SnO_2 inner layer, accompanied by a shrinkage of the inner hollow channels. With a further increase (decrease) of the proportion of tin precursor (mineral oil) in the core precursor solution, a solid coaxial structure could be obtained, as illustrated in Scheme 2.

3.5. Photocatalytic activity

In order to test the practical applicability of electrospun coaxial heterostructures, the photocatalytic activities of SnO_2/TiO_2 nanofibers were evaluated by monitoring the degradation of a typical organic dye. Fig. 7A highlights the degradation of RhB in the presence of tubular SnO_2/TiO_2 nanofiber photocatalysts under UV illumination over a time period of 150 min. By comparison, the photocatalytic activities of commercial TiO_2 nanoparticles (Degussa P25), electrospun TiO_2 nanofibers, as well as solid SnO_2/TiO_2 coaxial nanofibers were also tested under identical conditions. The data show that the degradation of RhB catalyzed by tubular SnO_2/TiO_2 nanofibers is faster than that associated with the three other types of photocatalysts, whereas the dye in the control experiment experiences little if any degradation upon UV exposure. The photocatalytic degradation reaction of RhB can be modeled as a pseudo-first-order reaction with the kinetics expressed by the equation, $\ln(C_0/C_t) = kt$, where C_0 represents the initial concentration of aqueous RhB, C_t denotes the concentration of RhB at a given reaction time "t", and k is the reaction rate constant.

Derived from the plot as shown in Fig. 7B, the computed reaction rate constants are 4.6×10^{-3}, 3.3×10^{-3}, 3.0×10^{-3} and 2.5×10^{-3} min^{-1} for tubular SnO_2/TiO_2 nanofibers, solid SnO_2/TiO_2 nanofibers, TiO_2 nanofibers and Degussa P25, respectively. In addition, the available surface area of tubular SnO_2/TiO_2 nanofibers was determined to be 87 m^2 g^{-1} (Table 4), which is noticeably higher than that of Degussa P25 TiO_2 nanoparticles (55 m^2 g^{-1}), solid TiO_2 nanofibers (52 m^2 g^{-1}), and solid SnO_2/TiO_2 nanofibers (60 m^2 g^{-1}), respectively. It has been suggested that rutile phase TiO_2 possesses a lower activity than its anatase analogue.[48] Therefore, it is not surprising that solid SnO_2/TiO_2 coaxial nanofibers with a pure rutile phase did not evidently lead to a significant enhancement in the activity as compared with its anatase counterpart. However, our tubular SnO_2/TiO_2

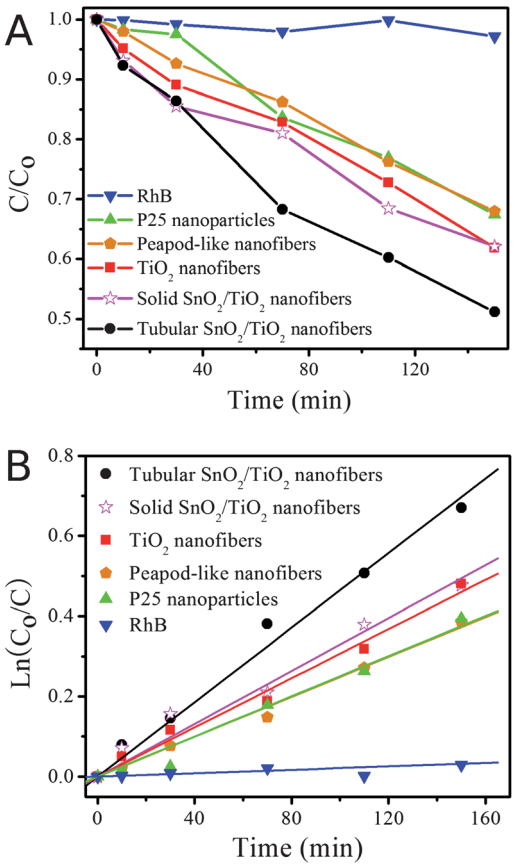

Fig. 7 (A) Degradation profiles of Rhodamine B (RhB) in the presence of different photocatalysts under UV illumination. (B) First-order kinetic rate constant data associated with RhB photocatalytic degradation in the presence of different photocatalysts.

nanofibers exhibited perceptibly improved photocatalytic performance as compared with either solid TiO_2 nanofibers or commercial TiO_2 nanoparticles alone, under identical reaction conditions. In fact, this noticeable improvement in the activity of tubular SnO_2/TiO_2 nanofibers can be attributed to a number of factors related to the unique structure of the fibers as well as to the energy level offset between SnO_2 and TiO_2, which is inherently beneficial for efficient charge separation at the interface of these two component structures.

First, nanoparticles spatially confined with nanofiber motifs likely experienced an efficient interparticle charge transport with its one-dimensional matrix. A comparison between Degussa P25 nanoparticles and pure TiO_2 fibers implied that interparticle interactions may play an important role in facilitating charge transport between the particles, thereby enhancing photocatalytic efficiency. Specifically, trapping and detrapping processes induced by the surface defects of randomly packed nanoparticles have been found to dramatically undermine charge mobility and subsequently cause significant charge recombination. In particular, studies have shown that one-dimensional structures encapsulating closely packed nanoparticles can enhance the diffusion length and improve the degree of charge transport.[49,50] For instance, the electrical conductivity of SnO_2 nanowires and polycrystalline nanotubes has been found to be more than five times higher than that of SnO_2 nanoparticles

Table 4 Measured physicochemical properties of different photocatalysts used in our study

Sample	BET surface area/m^2 g^{-1}	BJH pore radius/nm
Degussa P25 nanoparticles	55	1.4
Electrospun TiO_2 nanofibers	52	2.7
Solid SnO_2/TiO_2 nanofibers	60	2.0
Peapod-like SnO_2/TiO_2 nanofibers	70	2.0
Tubular SnO_2/TiO_2 nanofibers	87	2.7

alone.[51] A photocatalytic comparison between TiO_2 nanofibers and TiO_2 nanoparticles suggested that TiO_2 nanofibers possessed far higher photocatalytic activity by a factor of three in terms of photocurrent generation as a result of the noticeable improvement in interparticle charge transport.[24] Therefore, in our photocatalytic reactions, a rapid interparticle transport of photogenerated charge carriers through the grain boundaries in SnO_2/TiO_2 fibers likely accounts for the improved activities as compared with simply TiO_2 nanoparticles alone.

Second, the tubular structure led to a remarkable increase in accessible surface area. That is, the high surface area of tubular SnO_2/TiO_2 fibers allowed for a correspondingly high adsorption of active species, thereby promoting the observed photocatalytic efficiency. Third, photogenerated electron transfer from TiO_2 to SnO_2, due to the energy-level offset between the conduction bands of SnO_2 and TiO_2, greatly suppressed the possible recombination of charge carriers, as highlighted in Scheme 1B. As such, the tubular structure motif tended to facilitate the process wherein not only holes on TiO_2 but also electrons accumulated on SnO_2 could react with active species in solution, thereby providing oxidizing radicals that could subsequently act to assist in the degradation of organic dyes. We note that though the phase transformation of TiO_2 from anatase to rutile may lower its intrinsic photocatalytic activity, the synergistic coupling of the tubular one-dimensional structure with favorable electron transfer between TiO_2 and SnO_2 likely led to the overall observed enhancement of photocatalytic activity herein.

Of interest, we also find that the peapod-like SnO_2/TiO_2 nanofiber structure exhibited mediocre photocatalytic efficiency with a rate constant of 3.0×10^{-3} min^{-1}, which is comparable in behavior to that of Degussa P25 alone. This observation may be partially ascribed to the fact that the substantial presence of nanoparticles within these nanofibers might have blocked spatial accessibility of the reaction solution to the inner tube, therefore significantly reducing potential interactions between the active species and the SnO_2 component. Furthermore, as we have previously discussed, we expect a rapid interparticle transport of photogenerated charge carriers through the grain boundaries in solid SnO_2/TiO_2 fibers. By contrast, such facile electron transport would be less likely in these structurally more heterogeneous peapod-like SnO_2/TiO_2 architectures, wherein channels for electron movement would be inherently less straightforward to map out. That is, in these peapod-like structures, the accumulated charges at the SnO_2 layer may not have been effectively transported away from possible recombination sites. This plausible scenario, resulting from the relatively unordered presence of numbers of discrete SnO_2 nanoparticles within the hollow tubular TiO_2 channels, might therefore have led to a correspondingly inefficient extraction of photogenerated electrons, which would thereby have accounted for the lower than expected observed photocatalytic efficiency.

4. Conclusions

In summary, this study has demonstrated that SnO_2/TiO_2 nanofibers with well-defined core–shell structures can be readily fabricated by coaxial electrospinning. Three different interior morphologies could be prepared by appropriately varying the precursor concentration. Measurement of the photocatalytic activity of these materials has suggested that tubular coaxial nanofibers are superior to their compositional analogues as a result of the cumulative combination of the advantages associated with the formation of a heterojunction as well as a tubular motif. The established methodology reported herein is highly versatile and can be extended to different binary metal oxide systems, including SnO_2/Fe_2O_3[52] and ZnO/NiO,[53] as well as either metals or sulfides depending on appropriate post-treatments (*e.g.* annealing in a reducing atmosphere will generate metal nanofibers[54]). The important advantages of using coaxial electrospinning for the fabrication of inorganic heterostructures lie in its flexibility in terms of the choice of materials, synthetic simplicity, high yield, as well as the reliable generation of high-quality coaxial structures. Hence, the potential functionalities that can be incorporated into electrospun coaxial structures are essentially unlimited. In fact, these materials could readily encompass luminescent, magnetic, and ferroelectric moieties. Furthermore, the ability to tune the internal morphology of these one-dimensional nanostructures all the way from empty, hollow nanotubes to solid, filled nanowires may allow for the development of a host of useful applications.

Acknowledgements

Research (including support for SSW) was supported by the U.S. Department of Energy, Office of Basic Energy Sciences, Materials Sciences and Engineering Division. We also acknowledge that this work was done in part at the Center for Functional Nanomaterials at Brookhaven National Laboratory, supported by the Department of Energy under contract #DE-AC02-98CH10886. We also thank Dr Martin Schoonen for his assistance with the BET measurements, Dr James Quinn for his help with scanning electron microscopy, as well as Ms Susan van Horn and Ms Amanda Tiano for their efforts with transmission electron microscopy.

References

1 J. Xiang, W. Lu, Y. J. Hu, Y. Wu, H. Yan and C. M. Lieber, *Nature*, 2006, **441**, 489–493.
2 X. W. Teng, Q. Wang, P. Liu, W. Han, A. Frenkel, W. Wen, N. Marinkovic, J. C. Hanson and J. A. Rodriguez, *J. Am. Chem. Soc.*, 2008, **130**, 1093–1101.

3 X. W. Teng, M. Feygenson, Q. Wang, J. Q. He, W. X. Du, A. I. Frenkel, W. Q. Han and M. Aronson, *Nano Lett.*, 2009, **9**, 3177–3184.
4 Y. H. Lin, Y. C. Hsueh, P. S. Lee, C. C. Wang, J. R. Chen, J. M. Wu, T. P. Perng and H. C. Shih, *J. Electrochem. Soc.*, 2010, **157**, K206–K210.
5 M. Law, L. E. Greene, A. Radenovic, T. Kuykendall, J. Liphardt and P. D. Yang, *J. Phys. Chem. B*, 2006, **110**, 22652–22663.
6 Y. J. Dong, B. Z. Tian, T. J. Kempa and C. M. Lieber, *Nano Lett.*, 2009, **9**, 2183–2187.
7 Q. Kuang, Z. Y. Jiang, Z. X. Xie, S. C. Lin, Z. W. Lin, S. Y. Xie, R. B. Huang and L. S. Zheng, *J. Am. Chem. Soc.*, 2005, **127**, 11777–11784.
8 R. He, M. Law, R. Fan, F. Kim and P. Yang, *Nano Lett.*, 2002, **2**, 1109–1112.
9 C. L. Zhu, M. L. Zhang, Y. J. Qiao, G. Xiao, F. Zhang and Y. J. Chen, *J. Phys. Chem. C*, 2010, **114**, 16229–16235.
10 J. Jun, C. Jin, H. Kim, S. Park and C. Lee, *Appl. Surf. Sci.*, 2009, **255**, 8544–8550.
11 K. Nagashima, T. Yanagida, H. Tanaka, S. Seki, A. Saeki, S. Tagawa and T. Kawai, *J. Am. Chem. Soc.*, 2008, **130**, 5378–5382.
12 A. Datta, S. K. Panda and S. Chaudhuri, *J. Phys. Chem. C*, 2007, **111**, 17260–17264.
13 J. Cao, J.-Z. Sun, H.-Y. Li, J. Hong and M. Wang, *J. Mater. Chem.*, 2004, **14**, 1203–1206.
14 X. Q. Meng, H. Peng, Y. Q. Gai and J. Li, *J. Phys. Chem. C*, 2010, **114**, 1467–1471.
15 J. M. Wu, *J. Phys. Chem. C*, 2008, **112**, 13192–13199.
16 J. Hu, Y. Bando, Z. Liu, T. Sekiguchi, D. Golberg and J. Zhan, *J. Am. Chem. Soc.*, 2003, **125**, 11306–11313.
17 X. M. Shuai and W. Z. Shen, *J. Phys. Chem. C*, 2011, **115**, 6415–6422.
18 H. J. Fan, M. Knez, R. Scholz, K. Nielsch, E. Pippel, D. Hesse, M. Zacharias and U. Gosele, *Nat. Mater.*, 2006, **5**, 627–631.
19 J. Y. Park, S. W. Choi and S. S. Kim, *J. Phys. D: Appl. Phys.*, 2011, **44**, 205403.
20 J. Y. Park, S. W. Choi, J. W. Lee, C. Lee and S. S. Kim, *J. Am. Ceram. Soc.*, 2009, **92**, 2551–2554.
21 S. Ramakrishna, R. Jose, P. S. Archana, A. S. Nair, R. Balamurugan, J. Venugopal and W. E. Teo, *J. Mater. Sci.*, 2010, **45**, 6283–6312.
22 A. K. Moghe and B. S. Gupta, *Polym. Rev.*, 2008, **48**, 353–377.
23 R. Ramaseshan, S. Sundarrajan, R. Jose and S. Ramakrishna, *J. Appl. Phys.*, 2007, **102**, 111101.
24 S. K. Choi, S. Kim, S. K. Lim and H. Park, *J. Phys. Chem. C*, 2010, **114**, 16475–16480.
25 V. Thavasi, G. Singh and S. Ramakrishna, *Energy Environ. Sci.*, 2008, **1**, 205–221.
26 J. S. Chen, Z. Chen, R. Y. Chen, X. Zheng and X. Chen, *Acta Mater. Compos. Sin.*, 2011, **28**, 36–41.
27 A. L. Yarin, *Polym. Adv. Technol.*, 2011, **22**, 310–317.
28 Y. Z. Zhang, X. Wang, Y. Feng, J. Li, C. T. Lim and S. Ramakrishna, *Biomacromolecules*, 2006, **7**, 1049–1057.
29 H. L. Jiang, Y. Q. Hu, Y. Li, P. C. Zhao, K. J. Zhu and W. L. Chen, *J. Controlled Release*, 2005, **108**, 237–243.
30 Y. Yu, L. Gu, C. B. Zhu, P. A. van Aken and J. Maier, *J. Am. Chem. Soc.*, 2009, **131**, 15984–15985.
31 M. R. Hoffmann, S. T. Martin, W. Choi and D. W. Bahnemann, *Chem. Rev.*, 1995, **95**, 69–96.
32 L. R. Hou, C. Z. Yuan and Y. Peng, *J. Hazard. Mater.*, 2007, **139**, 310–315.
33 Z. Liu, D. D. Sun, P. Guo and J. O. Leckie, *Nano Lett.*, 2007, **7**, 1081–1085.
34 Y. Zhao, J. Liu, L. Y. Shi, S. A. Yuan, J. H. Fang, Z. Y. Wang and M. H. Zhang, *Appl. Catal., B*, 2010, **100**, 68–76.
35 K. Vinodgopal, I. Bedja and P. V. Kamat, *Chem. Mater.*, 1996, **8**, 2180–2187.
36 S. C. Ray, M. K. Karanjai and D. DasGupta, *Surf. Coat. Technol.*, 1998, **102**, 73–80.
37 Y. Liu, E. Koep and M. L. Liu, *Chem. Mater.*, 2005, **17**, 3997–4000.
38 D. G. Shchukin and R. A. Caruso, *Adv. Funct. Mater.*, 2003, **13**, 789–794.
39 J. Li and H. C. Zeng, *J. Am. Chem. Soc.*, 2007, **129**, 15839–15847.
40 K. K. Akurati, A. Vital, R. Hany, B. Bommer, T. Graule and M. Winterer, *Int. J. Photoenergy*, 2005, **7**, 153–161.
41 S. F. Chen, L. Chen, S. Gao and G. Y. Cao, *Mater. Chem. Phys.*, 2006, **98**, 116–120.
42 Y. Q. Cao, T. He, L. S. Zhao, E. J. Wang, W. S. Yang and Y. A. Cao, *J. Phys. Chem. C*, 2009, **113**, 18121–18124.
43 B. Liu and E. S. Aydil, *J. Am. Chem. Soc.*, 2009, **131**, 3985–3990.
44 D. Li and Y. N. Xia, *Nano Lett.*, 2004, **4**, 933–938.
45 D. Li, J. T. McCann and Y. N. Xia, *Small*, 2004, **1**, 83–86.
46 I. Robel, V. Subramanian, M. Kuno and P. V. Kamat, *J. Am. Chem. Soc.*, 2006, **128**, 2385–2393.
47 J. E. Díaz, A. Barrero, M. Márquez and I. G. Loscertales, *Adv. Funct. Mater.*, 2006, **16**, 2110–2116.
48 N. G. Park, J. van de Lagemaat and A. J. Frank, *J. Phys. Chem. B*, 2000, **104**, 8989–8994.
49 O. K. Varghese, M. Paulose and C. A. Grimes, *Nat. Nanotechnol.*, 2009, **4**, 592–597.
50 J. R. Jennings, A. Ghicov, L. M. Peter, P. Schmuki and A. B. Walker, *J. Am. Chem. Soc.*, 2008, **130**, 13364–13372.
51 M.-S. Park, Y.-M. Kang, G.-X. Wang, S.-X. Dou and H.-K. Liu, *Adv. Funct. Mater.*, 2008, **18**, 455–461.
52 M. T. Niu, F. Huang, L. F. Cui, P. Huang, Y. L. Yu and Y. S. Wang, *ACS Nano*, 2010, **4**, 681–688.
53 Z. Zhang, C. Shao, X. Li, C. Wang, M. Zhang and Y. Liu, *ACS Appl. Mater. Interfaces*, 2010, **2**, 2915–2923.
54 H. Wu, R. Zhang, X. X. Liu, D. D. Lin and W. Pan, *Chem. Mater.*, 2007, **19**, 3506–3511.

